Global Λ polarization in heavy-ion collisions at energies 2.4–7.7 GeV: Effect of meson-field interaction

Yu. B. Ivanov [1,2,3,*] and A. A. Soldatov [2]

[1] *Bogoliubov Laboratory for Theoretical Physics, Joint Institute for Nuclear Research, Dubna 141980, Russia*
[2] *National Research Nuclear University "MEPhI", Moscow 115409, Russia*
[3] *National Research Centre "Kurchatov Institute", Moscow 123182, Russia*

(Received 17 January 2022; accepted 17 March 2022; published 31 March 2022)

Based on the three-fluid model, the global Λ polarization in Au+Au collisions at $2.4 \leqslant \sqrt{s_{NN}} \leqslant 7.7$ GeV is calculated, including its rapidity and centrality dependence. Contributions from the thermal vorticity and meson-field term (proposed by Csernai, Kapusta, and Welle) to the global polarization are considered. The results are compared with data from recent and ongoing STAR and HADES experiments. It is predicted that the polarization maximum is reached at $\sqrt{s_{NN}} \approx 3$ GeV, if the measurements are performed with the same acceptance. The value of the polarization is very sensitive to interplay of the aforementioned contributions. In particular, the thermal vorticity results in quite strong increase of the polarization from the midrapidity to forward/backward rapidities, while the meson-field contribution considerably flattens the rapidity dependence. The polarization turns out to be very sensitive to details of the equation of state. While collision dynamics become less equilibrium with decreasing collision energy, the present approach to polarization is based on the assumption of thermal equilibrium. It is found that equilibrium is achieved at the freeze-out stage, but this equilibration takes longer at moderately relativistic energies.

DOI: 10.1103/PhysRevC.105.034915

I. INTRODUCTION

Measurements of polarization of particles produced in heavy-ion collisions give us access to a new class of collective phenomena, i.e., collective rotation of the nuclear medium. The STAR Collaboration at the Relativistic Heavy Ion Collider (RHIC) observed nonzero global polarization of Λ and $\bar{\Lambda}$ at collision energies $7.7 \leqslant \sqrt{s_{NN}} \leqslant 200$ GeV [1,2] and, recently, multistrange hyperons [3] at 200 GeV. Local polarization along the beam direction also was measured [4]. These measurements demonstrated rising of the global polarization with decreasing $\sqrt{s_{NN}}$.

The spin polarization below 7.7 GeV is less explored. While a simple extrapolation of this trend suggests that the global polarization continues to rise as $\sqrt{s_{NN}}$ decreases, we expect vanishing global polarization at $\sqrt{s_{NN}} = 2m_N$ due to the lack of system angular momentum. Therefore, a peak in global polarization should exist in the region $1.9 \leqslant \sqrt{s_{NN}} \leqslant 7.7$ GeV. Recent model calculations predict this peak in the different places: at $\sqrt{s_{NN}} \approx 3$ GeV [5,6] and at $\sqrt{s_{NN}} \approx 7.7$ GeV [7].

First data (some of them preliminary) on the global polarization of Λ were presented in Refs. [8–10] for energies 3 GeV, 7.2 GeV, and 2.4 GeV, respectively. The first two energy points are obtained within STAR fixed-target program (FXT-STAR) at RHIC [11], the third point by HADES Collaboration at GSI Helmholtzzentrum für Schwerionenforschung [12]. These data indicate that the peak in global polarization is reached certainly below the energy of 7.7 GeV.

In this paper we present calculations of the global Λ polarization at energies 2.4–7.7 GeV. This energy range covers the energies of the aforementioned FXT-STAR and HADES experiments, as well as of the forthcoming experiments at the Facility for Antiproton and Ion Research (FAIR) in Darmstadt [13] and Nuclotron-based Ion Collider fAcility (NICA) in Dubna [14].

The calculations are performed within the model of the three-fluid dynamics (3FD) [15] combined with thermodynamic approach to the particle polarization [16–18]. The simulations are done with three different equations of state (EoS's): a purely hadronic EoS [19] and two versions of the EoS with the deconfinement transition [20], i.e., a first-order phase transition (1PT) and a crossover one. The physical input of the present 3FD calculations is described in Ref. [21]. A brief report on this study has been already presented in Ref. [6]. Here we present results of refined and extended calculations, as described in Secs. III and IV. The thermodynamic approach based on hadronic degrees of freedom [16–18] well describes the global polarization of hyperons, as was demonstrated by its realizations in various hydrodynamical [22–29] and transport [30–36] models of heavy-ion collisions. Though, this thermodynamic approach faces some problems, e.g., in explaining the Λ-$\bar{\Lambda}$ splitting, see recent reviews in Ref. [37,38].

*yivanov@theor.jinr.ru

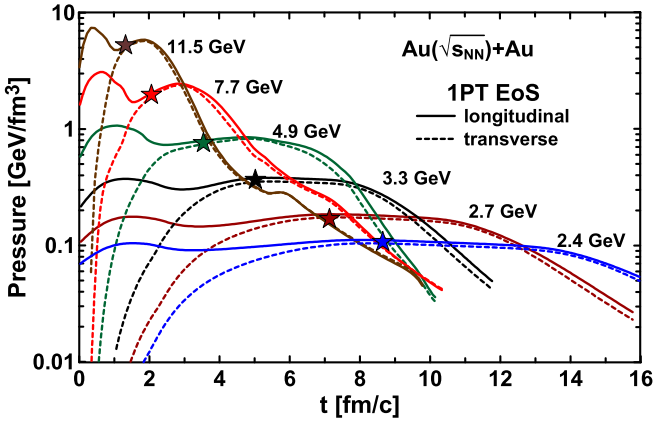

FIG. 1. Time evolution of the longitudinal and transverse pressure in the central region of Au+Au collision at various collision energies ($\sqrt{s_{NN}}$). The simulations are performed with the 1PT EoS. Star symbols on the curves mark the time instants of the mechanical equilibration.

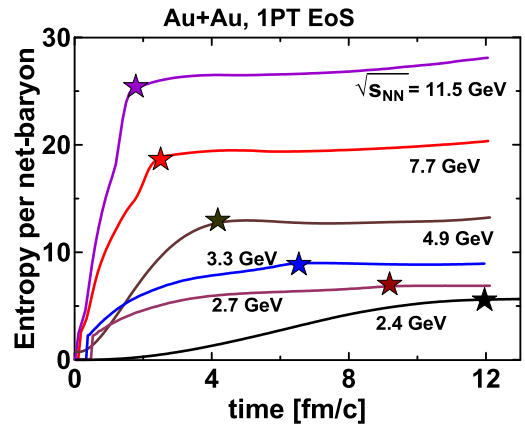

FIG. 2. Specific entropy per net baryon ($N_B = 2A = 394$) generated in Au+Au collisions at various energies $\sqrt{s_{NN}} = 2.4$-11.5 GeV within 1PT scenario [20] in the 3FD simulations. Star symbols on the curves mark time instants of the thermalization, i.e., those when the rapid growth of entropy is completed.

II. THERMALIZATION IN NUCLEAR COLLISIONS

The 3FD model takes into account nonequilibrium at the early stage of nuclear collisions. This nonequilibrium stage is modeled by means of two counterstreaming baryon-rich fluids (p and t fluids). Newly produced particles, dominantly populating the midrapidity region, are attributed to a fireball (f) fluid. These fluids are governed by conventional hydrodynamic equations coupled by friction terms in the right-hand sides of the Euler equations.

The model [16–18] used to calculate the global polarization of Λ is based on thermodynamic concepts. At moderately relativistic energies, the thermalization of the matter of colliding nuclei is slow and hence the early nonequilibrium stage of nuclear collisions can be quite long. Therefore, before proceeding to model predictions it is instructive to consider degree of the thermalization of the matter at the freeze-out stage. Mechanical equilibration in the center region of colliding nuclei was studied in Ref. [39]. Criterion of the mechanical equilibration is equality of longitudinal and transverse pressures with the accuracy no worse than 10%. It is relevant to the nuclear collisions because the leading inequilibrium at the initial stage of the collision is associated with anisotropy of the momentum distribution along and transverse the beam direction. Time evolution of these pressure components in the central region of Au+Au collision at various collision energies ($\sqrt{s_{NN}}$) is displayed in Fig. 1. The simulations are performed with the 1PT EoS. Time instants, when the equilibration happens, are marked by star symbols on the curves in Fig. 1.

A peculiar time evolution of the pressure at the energy of 11.5 GeV (see wiggle $t = 5$–6 fm/c) is a signal of the mixed phase through which the system passes. At 7.7 GeV, the mixed phase manifests itself only as a weak irregularity in the evolution, since the system quickly passes this phase. Results with the crossover EoS are very similar, of course, without these irregularities.

As seen, the mechanical equilibration is indeed slow at the moderately relativistic energies, see Fig. 1. However, even at $\sqrt{s_{NN}} = 2.42$ GeV it is reached (≈ 9 fm/c) to the freeze-out stage. The freeze-out stage is extended in time, though it is completed at ≈ 20 fm/c from the beginning of the collision. The end points of the evolution curves in Fig. 1 correspond to the end of the freeze-out stage. The mechanical equilibration is of prime importance for applicability of the thermodynamic model [16–18].

The chemical equilibration and thus thermalization takes longer. Evolution of entropy [40] (Fig. 2) shows that at $\sqrt{s_{NN}} = 2.42$ GeV the thermalization takes place at $\approx$12 fm/c. Estimation of the thermalization within other models [41–45] also indicates that it takes long time, i.e., of the order of that in the 3FD or even longer, but it is completed before the freeze-out stage. The success of the statistical model [46] at moderate energies also indicates the thermalization at the freeze out.

III. GLOBAL POLARIZATION IN 3FD MODEL

In the thermodynamic approach [16–18], particle polarization is related to so-called thermal vorticity defined as

$$\varpi_{\mu\nu} = \tfrac{1}{2}(\partial_\nu \beta_\mu - \partial_\mu \beta_\nu), \tag{1}$$

where $\beta_\mu = u_\nu/T$, u_μ is collective local four-velocity of the matter, and T is local temperature. Here we deal with u_μ and T of the unified fluid because the system is equilibrated at the freeze-out stage, as argued in the previous section. In the leading order in the thermal vorticity it is directly related to mean spin vector of spin 1/2 particles with four-momentum p, produced around point x on freeze-out hypersurface

$$S^\mu(x, p) = \frac{1}{8m}[1 - n_F(x, p)]\, p_\sigma \epsilon^{\mu\nu\rho\sigma} \varpi_{\rho\nu}(x), \tag{2}$$

where $n_F(x, p)$ is the Fermi-Dirac distribution function and m is mass of the considered particle. The polarization vector of

S-spin particle is defined as

$$P_S^\mu = S^\mu / S. \tag{3}$$

The polarization of the Λ hyperon is measured in its rest frame, therefore the Λ polarization is

$$P_\Lambda^\mu = 2 S_\Lambda^{*\mu}, \tag{4}$$

where $S_\Lambda^{*\mu}$ is mean spin vector of the Λ hyperon in its rest frame. The zeroth component S_Λ^0 identically vanishes in the Λ rest frame and the spatial component becomes [34]

$$\mathbf{S}_\Lambda^*(x,p) = \mathbf{S}_\Lambda - \frac{\mathbf{p}_\Lambda \cdot \mathbf{S}_\Lambda}{E_\Lambda (E_\Lambda + m_\Lambda)} \mathbf{p}_\Lambda, \tag{5}$$

where $E_\Lambda = \sqrt{m_\Lambda^2 + \mathbf{p}^2}$. Substitution of the expression for $\mathbf{S}$ from Eq. (2) and averaging this expression over the $\mathbf{p}_\Lambda$ direction (i.e., over $\mathbf{n}_p$) results in the following polarization in the direction orthogonal to the reaction plane (xz) [34]

$$\langle P_\Lambda \rangle_{\mathbf{n}_p} = \frac{1}{2 m_\Lambda} \left(E_\Lambda - \frac{1}{3} \frac{\mathbf{p}_\Lambda^2}{E_\Lambda + m_\Lambda} \right) \varpi_{zx}, \tag{6}$$

where m_Λ is the Λ mass, E_Λ and $\mathbf{p}_\Lambda$ are the energy and momentum of the emitted Λ hyperon, respectively. Here we put $(1 - n_\Lambda) \simeq 1$ because the Λ production takes place only in high-temperature regions, where Boltzmann statistics dominate.

Particles are produced across entire freeze-out hypersurface. Therefore to calculate the global polarization vector, the above expression should be averaged over the freeze-out hypersurface Σ and particle momenta

$$P_\Lambda^\varpi = \frac{\int (d^3p/p^0) \int_\Sigma d\Sigma_\lambda p^\lambda n_\Lambda \langle P_\Lambda \rangle_{\mathbf{n}_p}}{\int (d^3p/p^0) \int_\Sigma d\Sigma_\lambda p^\lambda n_\Lambda}. \tag{7}$$

Here P_Λ is averaged over the whole system and momenta of emitted particles. Application of the experimental rapidity acceptance is performed in terms of a so-called hydrodynamical rapidity

$$y_h = \frac{1}{2} \ln \frac{u^0 + u^3}{u^0 - u^3}, \tag{8}$$

based on hydrodynamical four-velocity u^μ. The $d\Sigma_\lambda p^\lambda$ integration runs only over those cells, where condition $|y_h| < y_{\text{acceptance}}$ is met. Let us denote this restricted freeze-out hypersurface as $\Sigma_{\Delta y}$. Of course, this is only imitation of the actual experimental acceptance. Unfortunately, imitation of transverse-momentum acceptance in the similar manner is impossible because the transverse momentum is mainly determined by thermal motion in the cell.

Similarly to previous 3FD simulations [6,25–27], a simplified version of the freeze out is used. The freeze out is isochronous that, in particular, implies $(d^3p/p^0) d\Sigma_\lambda p^\lambda = d^3p\, d^3x$. The freeze-out instant is associated with time, when the energy density $\langle \varepsilon(t) \rangle$ averaged over the central region (i.e., slab $|z| \leqslant 4$ fm) reaches the value of the average freeze-out energy density in the same central region obtained in conventional 3FD simulations with differential, i.e., cell-by-cell, freeze out [47,48]. This actual freeze-out energy density, ε_{frz}, averaged over frozen out system, is illustrated in Fig. 3 for two impact parameters and different EoS's. It is important

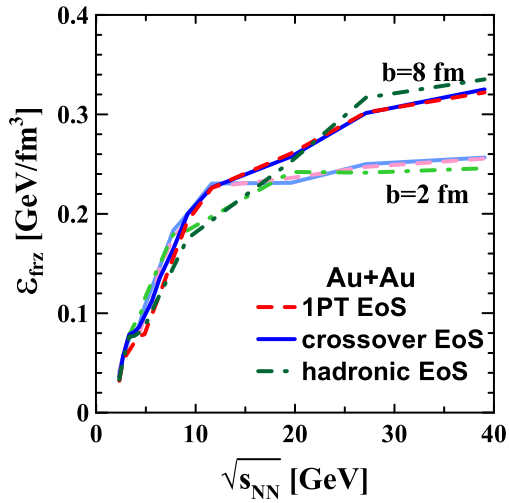

FIG. 3. Average actual freeze-out energy density versus collision energy $\sqrt{s_{NN}}$ in Au+Au collisions at impact parameters $b = 2$ and 8 fm calculated with different EoS's. Lower set of (pale) lines corresponds to $b = 2$ fm.

to note that values of ε_{frz} in Fig. 3 are not parameters of the 3FD model. They are automatically generated in the 3FD simulations as a result of the implemented freeze-out dynamics described in Refs. [47,48]. The only freeze-out parameter is $\epsilon_{\text{frz}} = 0.4$ GeV/fm^3, which has a meaning of a trigger energy density, at which the freeze-out procedure starts. This parameter is the same for all EoS's and all collision energies.

We can simplify Eq. (7) by explicitly performing integration over dp. We reorganize terms in parentheses in Eq. (6) and use the following relations:

$$\int d^3p\, d^3x\, n_\Lambda = \int d^3x\, \rho_\Lambda \tag{9}$$

$$\int d^3p\, d^3x\, E_\Lambda\, n_\Lambda = \int d^3x\, T_\Lambda^{00}, \tag{10}$$

where ρ_Λ is the Λ density in the frame of calculation and T_Λ^{00} is the 00 component of the partial energy-momentum tensor related to the Λ contribution

$$T_\Lambda^{00} = (\varepsilon_\Lambda + p_\Lambda) u^0 u^0 - p_\Lambda \tag{11}$$

with ε_Λ and p_Λ being the corresponding partial energy density and pressure, respectively. ρ_Λ, ε_Λ, and p_Λ are determined by ideal-gas relations in terms of temperature, baryon, and strange chemical potentials. Note that the system is described by the ideal-gas EoS at the freeze-out stage. Thus, inserting expression (6) for $\langle P_\Lambda \rangle_{\mathbf{n}_p}$ into Eq. (7) and performing the above-described manipulations we arrive at

$$P_\Lambda^\varpi = \frac{1}{6} \frac{\int_{\Sigma_{\Delta y}} d^3x (\rho_\Lambda + 2 T_\Lambda^{00}/m_\Lambda) \varpi_{zx}}{\int_{\Sigma_{\Delta y}} d^3x\, \rho_\Lambda}. \tag{12}$$

This is the final expression with which we perform our simulations.

In previous calculations [6,25–27], the n_Λ weight in Eq. (7) was replaced by the energy-density weight. Moreover, averaging of ϖ_{zx} and the term in parentheses in Eq. (6) was

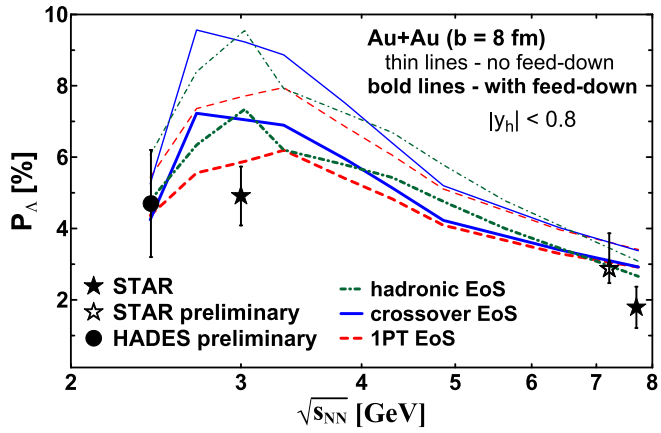

FIG. 4. Global Λ polarization in midrapidity region ($|y_h| < 0.8$), originated from the thermal vorticity, in Au+Au collisions at $b = 8$ fm as function of collision energy $\sqrt{s_{NN}}$ calculated with different EoS's. Result with contribution of the feed down from higher-lying resonances (bold lines) and without them (thin lines). Data are from Refs. [1,8,9] (STAR) and [10] (HADES).

decoupled. In the present approach we avoid these approximations.

A. Polarization transfer in two-body decays

Only a fraction of all detected Λ's are produced directly at the freeze-out stage. These are primary Λ's. A fraction of Λ's originates from decays of heavier hyperons. The most important feed-down channels are strong decays of $\Sigma^* \to \Lambda + \pi$ and electromagnetic decays $\Sigma^0 \to \Lambda + \gamma$. When polarized particles decay, their daughters are themselves polarized because of angular momentum conservation. The amount of polarization that is transferred to the daughter particle depends on the momentum of the daughter in the rest frame of the parent. For the mean, momentum-integrated, spin vector in the rest frame, a simple linear rule applies

$$\mathbf{S}^*_D = C\mathbf{S}^*_P, \tag{13}$$

where P is the parent particle, D is the daughter and C is a coefficient, values of which are presented in Table I of Ref. [17]. Making use of these C coefficients, we arrive at the following expression for the observable Λ polarization:

$$(P^{\varpi}_{\Lambda})_{\rm obs.} = \frac{N_\Lambda P^{\varpi}_{\Lambda} + (5/3)N_{\Sigma^*}P^{\varpi}_{\Sigma^*} - (1/3)N_{\Sigma^0}P^{\varpi}_{\Sigma^0}}{N_\Lambda + N_{\Sigma^*} + N_{\Sigma^0}}, \tag{14}$$

where P^{ϖ}_{Y} is the global polarization Y hyperon ($Y = \Lambda, \Sigma^*, \Sigma^0$) calculated similarly to Eq. (12) and

$$N_Y = \int_{\Sigma_{\Delta y}} d^3x\, \rho_Y \tag{15}$$

is the total number of Y hyperons ($Y = \Lambda, \Sigma^*, \Sigma^0$) on the freeze-out hypersurface $\Sigma_{\Delta y}$. In Eq. (15) we neglected contribution of the decay channel $\Sigma^* \to \Sigma + \pi$ with small branching ratio (0.117), and hence put the branching ratio of the $\Sigma^* \to \Lambda + \pi$ channel equal to unit.

In Fig. 4 we demonstrate the effect of the feed down from higher-lying resonances on the global Λ polarization in midrapidity region ($|y_h| < 0.8$). The impact parameter $b = 8$ fm roughly roughly comply with the STAR centrality selection of 20–50% [1]. To associate these impact parameters with collision centrality, one should keep in mind that in the 3FD model the colliding nuclei have a shape of sharp spheres without the Woods-Saxon diffuse edge. This fact, implemented in the Glauber simulations based on the nuclear overlap calculator [49], results in this mean impact parameter, which is shifted by ≈1.5 fm down, as compared the result of Ref. [50]. The width of this midrapidity region is chosen on the condition of the best reproduction of the STAR acceptance $|\eta| < 1$ [1], where η is pseudorapidity. This window is not that good for the low-energy data [8–10], where rapidity acceptance is asymmetric with respect to the midrapidity. However, it is still good in view of flat rapidity dependence of the observed P_Λ. Results are presented for three EoS's. As seen, the feed down reduces P_Λ by ≈25% at low energies and by ≈15% at 7.7 GeV. All results presented below are calculated taking into account feed down from higher-lying resonances.

IV. MESON-FIELD INDUCED POLARIZATION

In this section, meson-field-induced contribution to the global polarization is discussed. It was proposed in Ref. [51] primarily to explain the observed Λ-$\bar{\Lambda}$ splitting in the global polarization. We do not discuss this splitting in the present paper because it deserves special separate discussion, but rather study the effect of the meson-field-induced contribution on the Λ polarization. Below, we briefly repeat derivation of Refs. [51,52] with the same result but somewhat different reasoning.

Let strong interaction among baryons be mediated by a scalar field σ and a vector field V^μ, as it assumed in the Walecka model [53,54]. The effective Lagrangian of this model is

$$\mathcal{L}_{\rm eff} = \sum_j \bar{\psi}_j (i\partial\!\!\!/ - m_j + g_{\sigma j}\sigma - g_{Vj} V\!\!\!/)\psi_j + \frac{1}{2}\left(\partial_\mu\sigma\,\partial^\mu\sigma - m_\sigma^2\sigma^2\right) - \frac{1}{4}V^{\mu\nu}V_{\mu\nu} + \frac{1}{2}m_V^2 V_\mu V^\mu. \tag{16}$$

Here j labels the spin-1/2 baryons, and the field strength tensor for the vector field is

$$V_{\mu\nu} = \partial_\mu V_\nu - \partial_\nu V_\mu. \tag{17}$$

In general, the Lagrangian may include a potential $U(\sigma)$ of σ-field self-interaction, but its exact form is irrelevant here. Therefore, we put $U(\sigma) = 0$ for definiteness. The V field is usually associated with the vector ω meson and σ, with the σ meson. The σ field results in an attractive interaction and ω, a repulsive interaction. $g_{\omega j}$ and $g_{\sigma j}$ are the coupling constants, possible values of which can be found, e.g., in Ref. [55].

The σ and ω fields are treated in the mean-field approximation [53–55]:

$$\partial^2 V^\nu + m_V^2 V^\nu = \sum_j g_{Vj} J^\nu_j, \tag{18}$$

where $J_j^\mu = \langle \bar{\psi}\gamma^\mu\psi\rangle$ is the baryon current of j baryons, in which baryons and antibaryons contribute with opposite signs, and

$$\partial^2\sigma + m_\sigma^2\sigma = \sum_j g_{\sigma j} n_{sj}, \tag{19}$$

where $n_{sj} = \langle\bar{\psi}\psi\rangle$ is the scalar density, in which baryons and antibaryons contribute with the same signs. It is expected that these interactions in terms of hadrons are relevant at the freeze-out stage even if the preceding evolution was dominated by the quark-gluon phase. At this stage the corresponding energy scale is much less than $m_\omega = 783$ MeV and $m_\sigma \approx 600$ MeV. Therefore, the derivatives in Eqs. (18) and (19) can be neglected, and thus we arrive at the following solution for the fields:

$$\sigma = \frac{1}{m_\sigma^2}\sum_j g_{\sigma j} n_{sj}, \tag{20}$$

$$V^\nu = \frac{1}{m_V^2}\sum_j g_{Vj} J_j^\nu \simeq \frac{\bar{g}_V}{m_V^2} J_B^\nu. \tag{21}$$

The V^ν field can be approximately expressed through the baryon current $J_B^\nu = n_B u^\nu$, where n_B is the baryon density and $\bar{g}_V$ is the mean coupling constant of the vector meson.

Nonrelativistic reduction of the interaction between the fields and the spin operator $\widehat{\mathbf{S}}$ of the Λ and $\bar{\Lambda}$ hyperons is performed by means of the Foldy-Wouthuysen transformation [56–58], i.e., an expansion in powers of the inverse of baryon masses, which complies with neglecting derivatives in Eqs. (18) and (19). The nonrelativistic interaction of the spin with the meson fields reads

$$\begin{aligned}\widehat{H}_{\rm spin} = {}& \frac{g_{\sigma\Lambda}}{2m_\Lambda^2}\widehat{\mathbf{S}}\cdot\nabla\sigma\times\widehat{\mathbf{p}} - \frac{g_{V\Lambda}}{m_\Lambda}\beta\widehat{\mathbf{S}}\cdot\mathbf{B}_V \\ & - i\frac{g_{V\Lambda}}{4m_\Lambda^2}\widehat{\mathbf{S}}\cdot\nabla\times\mathbf{E}_V - \frac{g_{V\Lambda}}{2m_\Lambda^2}\widehat{\mathbf{S}}\cdot\mathbf{E}_V\times\widehat{\mathbf{p}}.\end{aligned} \tag{22}$$

Here $\mathbf{E}_V$ and $\mathbf{B}_V$ are the vector-meson electric and magnetic fields

$$E_i = V_{i0}, \tag{23}$$

$$B_i = -\tfrac{1}{2}\varepsilon_{ijk}V^{jk}, \tag{24}$$

where $i, j, k = 1, 2, 3$, $\widehat{\mathbf{p}}$ is the momentum operator of the Λ or $\bar{\Lambda}$, and

$$\beta = \begin{pmatrix} 1 & 0 \\ 0 & -1 \end{pmatrix} \tag{25}$$

is the usual Dirac 4×4 β matrix, resulting in opposite signs when acting on the Λ and $\bar{\Lambda}$ spinors.

Let us turn to the density operator

$$\widehat{\rho} = \frac{1}{Z}\exp[-\widehat{H}/T + \nu\widehat{Q}/T + \boldsymbol{\omega}\cdot(\widehat{\mathbf{L}} + \widehat{\mathbf{S}})/T], \tag{26}$$

where $\widehat{H}$ is the Hamiltonian, T is the temperature, $\widehat{Q}$ stands for conserved charges (baryon, electric, strangeness) with ν being the corresponding chemical potentials. The angular velocity $\boldsymbol{\omega}$ plays the role of a chemical potential for the angular momentum, consisting of the orbital ($\widehat{\mathbf{L}}$) and spin ($\widehat{\mathbf{S}}$) parts.

Inspecting the spin-dependent part of the Hamiltonian, Eq. (22), we see that only the second and third terms on the right-hand side can be associated with additional corrections to the spin chemical potential, provided the equilibrium is local. The first and fourth terms also produce the polarization, but a chaotic one, because its direction depends on the momentum direction. However, they may induce a collective polarization, if there is a strong collective flow, i.e., if particle momenta are dominantly aligned along certain direction. This polarization would be similar to that discussed in Refs. [59–61]. The third term contains the extra derivative in the nominator and the extra Λ mass (m_Λ) in the denominator, as compared to the second term. This combination amounts to a smallness parameter, which has been already used when neglecting derivatives in the mean-field equations (18) and (19). Besides, only the sum of the third and fourth terms in Eq. (23) is Hermitian, not the individual terms. Therefore, it is reasonable to disregard them together. Thus, we can represent the density operator relevant to the global polarization in the following form:

$$\widehat{\rho} = \frac{1}{Z}\exp\left[-\frac{\widehat{\widetilde{H}}}{T} + \frac{\nu}{T}\widehat{Q} + \frac{g_{V\Lambda}}{m_\Lambda T}\beta\widehat{\mathbf{S}}\cdot\boldsymbol{B}_V + \frac{\boldsymbol{\omega}}{T}\cdot(\widehat{\mathbf{L}} + \widehat{\mathbf{S}})\right], \tag{27}$$

where the term with the extra spin chemical potential from $\widehat{H}_{\rm spin}$ is explicitly displayed, while $\widehat{\widetilde{H}}$ denotes the rest part of the Hamiltonian.

Derivation along the lines of Ref. [62] results in the mean spin vector of the hyperons ($Y = \Lambda$ or $\bar{\Lambda}$) with four-momentum p, produced around point x

$$S_Y^\mu(x, p) = \frac{1}{4}\left(\varpi_{\rm c}^\mu + \beta_Y\frac{g_{V\Lambda}}{m_\Lambda T}B_V^\mu\right), \tag{28}$$

where $\beta_\Lambda = 1$ and $\beta_{\bar{\Lambda}} = -1$,

$$\varpi_{\rm c}^\mu = -\tfrac{1}{2}\epsilon^{\mu\rho\sigma\tau}\varpi_{\rho\sigma}p_\tau/m_\Lambda \tag{29}$$

is the comoving axial thermal vorticity defined in terms of the thermal vorticity (1). Here we returned to the relativistic treatment of the rotation, therefore the angular velocity $\boldsymbol{\omega}$ was replaced by the relativistic thermal vorticity. We can make expression (28) completely covariant by identifying the magnetic field B_V^μ with the comoving magnetic field

$$B_V^\mu = B_c^\mu = -\epsilon^{\mu\rho\sigma\tau}V_{\rho\sigma}p_\tau/m_\Lambda. \tag{30}$$

This is a certain ansatz because the corresponding interaction (22) was originally derived in the nonrelativistic approximation. In explicitly covariant form Eq. (28) reads

$$S_Y^\mu(x, p) = -\frac{1}{8m_\Lambda}\epsilon^{\mu\rho\sigma\tau}p_\tau\left(\varpi_{\rho\sigma} + \beta_Y\frac{g_{V\Lambda}}{m_\Lambda T}V_{\rho\sigma}\right). \tag{31}$$

The vector meson field enters this expression similarly to the electromagnetic field interacting with magnetic moment of the Y hyperon [17]. This expression is valid [62] (see also Ref. [17]) in the leading order in the thermal vorticity and field strength tensor. The Fermi factor $[1 - n_Y(x, p)]$ was again omitted because of its negligible effect at high temperatures achieved in nuclear collisions.

The further derivation is identical to that performed in the previous section with the substitution $(\varpi_{\rho\sigma} + \beta_Y \frac{g_{V\Lambda}}{m_\Lambda T} V_{\rho\sigma})$ instead of $\varpi_{\rho\sigma}$. Finally we arrive to the following expression for the meson-field contribution to the global polarization of the Y hyperon ($Y = \Lambda$ or $\bar{\Lambda}$):

$$P_Y^V = \frac{\beta_Y g_{V\Lambda}}{6 m_\Lambda T} \frac{\int_{\Sigma_{\Delta y}} d^3x (\rho_Y + 2T_Y^{00}/m_\Lambda) V_{zx}}{\int_{\Sigma_{\Delta y}} d^3x\, \rho_Y}, \tag{32}$$

which should be added to the thermal-vorticity term (12). Here $\beta_\Lambda = 1$ and $\beta_{\bar{\Lambda}} = -1$, and V_{zx} is defined in terms of the baryon current, J_B^ν, by Eq. (21). The feed-down correction (14) should be applied to the sum of thermal-vorticity and meson-field terms.

For practical calculations the coupling constant $g_{V\Lambda}$ and the mean coupling constant $\bar{g}_V$ of the vector meson are needed. A brief survey of various parametrizations of the relativistic mean-field (RMF) model is presented in Ref. [51], see also [63,64]. We use just one of the possible parametrizations: $\bar{g}_V = g_{VN} = 8.646$, $g_{V\Lambda} = 0.67 g_{VN}$, and $m_V = m_\omega = 783$ MeV [65]. The mean coupling constant is associated with the nucleon one because nucleons dominate in the baryonic content of system at low energies considered here. The uncertainty in the RMF-model parametrization results in the corresponding uncertainty in the P_Y^V calculation.

To estimate the scale of the additional V term, we present the terms in parentheses in Eq. (31) as follows:

$$\varpi_{zx} + \frac{g_{\omega\Lambda}}{m_\Lambda T} V_{zx} = \varpi_{zx} + \left(\frac{g_{\omega\Lambda} \bar{g}_\omega n_0}{m_\Lambda m_\omega^2} \right) \frac{J_{zx}^B}{T n_0}, \tag{33}$$

where $n_0 = 0.15$ fm $- 3$ is the normal nuclear density and

$$J_{\mu\nu}^B = \partial_\mu J_\nu^B - \partial_\nu J_\mu^B \tag{34}$$

is vorticity of the baryon current, see Eq. (21). The factor

$$\frac{g_{\omega\Lambda} \bar{g}_\omega n_0}{m_\Lambda m_\omega^2} \approx 0.1 \tag{35}$$

is a natural scale of the additional V term. In practice, the contribution of the V term can be greater (up to several tens of percent) or less (down to several percent) or even have the opposite sign, depending on spatial distributions of thermal and baryon-current vorticities and values of the baryon density at the freeze out.

Figure 5 demonstrates the effect of the meson-field contribution to the global Λ polarization. As seen, the additional meson-field term considerably reduces the Λ polarization in rapidity window $|y_h| < 0.8$ at low collision energies and makes it closer to the STAR data at 3 GeV [8]. At the same time this effect is small in narrower window $|y_h| < 0.4$. This is a result of the aforementioned spatial distributions of thermal and baryon-current vorticities. In Fig. 6, the spatial distributions of the proper-energy-density weighted relativistic baryon-current zx vorticity, the similarly weighted thermal zx vorticity, the temperature, and the proper baryon density in the reaction plane (xz) at time instant $t = 16$ fm/c in the semicentral ($b = 8$ fm) Au+Au collision at $\sqrt{s_{NN}} = 2.7$ GeV are presented. Calculations are performed with the crossover EoS. This time instant of $t = 16$ fm/c is close to the freeze-out time (16.8 fm/c) determined by means of the average freeze-out

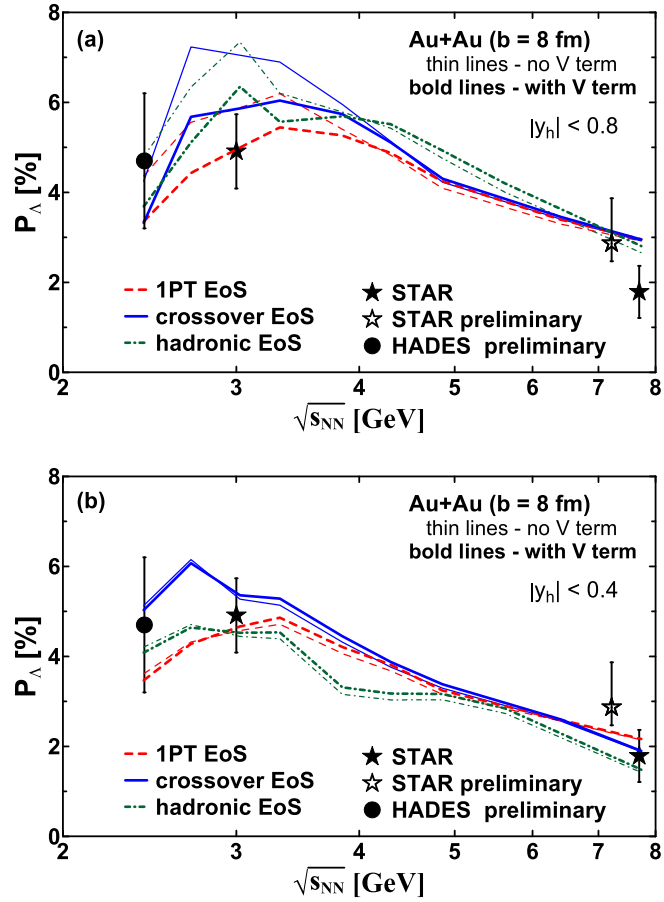

FIG. 5. Global Λ polarization in midrapidity regions (a) $|y_h| < 0.8$ and (b) $|y_h| < 0.4$, originated from the thermal vorticity with (bold lines) and without (thin lines) the meson-field contribution, in Au+Au collisions at $b = 8$ fm as function of collision energy $\sqrt{s_{NN}}$. Results for different EoS's are presented. Data are from Refs. [1,8,9] (STAR) and [10] (HADES).

energy density in the central region obtained in conventional 3FD simulations, see Fig. 3.

Approximate borders of the regions corresponding to restrictions on the hydrodynamical rapidity y_h, see Eq. (8), are displayed by gray boxes in the $J_{zx}^B/(n_0 T)$ panel of Fig. 6: $|y_h| < 0.8$ by the light-colored box and $|y_h| < 0.4$ by the dark-colored box). As seen, the baryon-current zx vorticity and the thermal zx one achieve highest absolute values at the participant-spectator border. Moreover, these values are of the opposite sign. The near-border absolute value of $J_{zx}^B/(n_0 T)$ exceeds that of ϖ_{zx}. Panels (T) and (n_B/n_0) of Fig. 6 demonstrate that gradients of $1/T$ and n_B/n_0 also essentially contribute to ϖ_{zx} and $J_{zx}^B/(n_0 T)$, respectively, rather than only vortical motion of the matter.

The $|y_h| < 0.8$ region almost completely includes the participant-spectator border. Therefore, the $(|y_h| < 0.8)$-region integrated baryon-current vorticity [multiplied by 0.1, see (35)] considerably reduces the ϖ_{zx} polarization. The $|y_h| < 0.4$ region only slightly overlaps with the participant-spectator border. Hence, the main contribution to the meson-field contribution to the global polarization comes from the

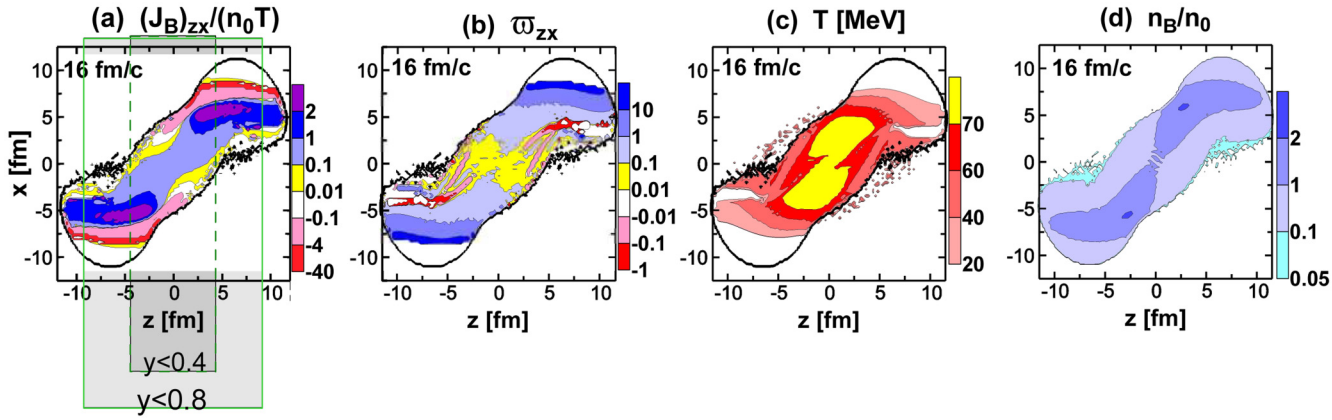

FIG. 6. Panels from left to right: (a) $J^B_{zx}/(n_0T)$, the proper-energy-density weighted relativistic baryon-current zx vorticity, Eq. (34), divided by temperature (T) and normal nuclear density (n_0), (b) ϖ_{zx}, the similarly weighted thermal zx vorticity, (c) T, the temperature, and (d) n_B/n_0, the proper baryon density in units of the normal nuclear density (n_0) in the reaction plane (xz) at time instant $t = 16$ fm/c in the semicentral ($b = 8$ fm) Au+Au collision at $\sqrt{s_{NN}} = 2.7$ GeV. Calculations are done with the crossover EoS. z axis is the beam direction. Gray-shaded boxes in the $J^B_{zx}/(n_0T)$ panel indicate approximate borders of the midrapidity regions $|y_h| < 0.8$ (light-gray outer box) and $|y_h| < 0.4$ (dark-gray inner box), where y_h is the hydrodynamical rapidity, see Eq. (8).

bulk, where the baryon-current vorticity is quite moderate. Therefore, the V correction to the global polarization in the $|y_h| < 0.4$ region is small.

The effect of the meson-field contribution is negligible at higher energies even in the ($|y_h| < 0.8$) window, see Fig. 5. The Λ polarization sometimes even increases, though only slightly, because of the meson-field contribution. In particular, it means that the meson-field-induced polarization does not explain the Λ-$\bar{\Lambda}$ splitting at the energy of 7.7 GeV. This is in contrast to results of Ref. [52], where it did explain. The reason is twofold. First, the ($|y_h| < 0.8$) window becomes too narrow to cover the participant-spectator border, where the baryon-current vorticity and the thermal one achieve highest absolute values. Second, the baryon density at the freeze out decreases with the collision energy rise. Indeed, the peak value of the baryon density in the ($|y_h| < 0.8$) window at the freeze out occurs precisely at these low collision energies at $b = 8$ fm, as seen from Fig. 7. This peak is achieved, in particular, because the spectator regions are partially included in this ($|y_h| < 0.8$) region. It seemingly contradicts the results by Cleymans and Randrup [66], obtained in the statistical model. They obtained the maximum baryon density at approximately 8 GeV, when analyzing central collisions. The 3FD model predicts a similar result for the central collisions: the maximum n_B is achieved at ≈ 8 GeV at $b = 2$ fm, see Fig. 7.

V. RAPIDITY DEPENDENCE

The STAR data [8] on rapidity dependence of the global Λ polarization at $\sqrt{s_{NN}} = 3$ GeV are presented for a wide range of centrality selection 0–50 %. The nuclear overlap calculator [49], based on the Glauber simulations, predicts the range of impact parameters $b = 0$–8.8 fm for this centrality range. This estimate takes into account that the colliding nuclei are sharp spheres without the Woods-Saxon diffuse edge in the 3FD model. Such a wide range cannot be represented by a single impact parameter. Therefore, we need to perform averaging over b:

$$\langle P_\Lambda \rangle = \int_0^{b_{\max}} bdb\, P_\Lambda(b) \Big/ \int_0^{b_{\max}} bdb, \tag{36}$$

where $b_{\max} = 8.8$ fm. Actual 3FD simulations of Au+Au collisions were performed at discrete impact parameters $b = 2$, 4, 6, 8, and 11 fm. Therefore, we replace the integral in Eq. (36) by a sum over impact parameters

$$\langle P_\Lambda \rangle \approx \sum_{b_i=2,4,6,8\text{fm}} b_i\, P_\Lambda(b_i) \Big/ \sum_{b_i=2,4,6,8\text{fm}} b_i, \tag{37}$$

where Δb is canceled because b_i points are equidistant.

The rapidity dependence of the global Λ polarization at 3 GeV, calculated accordingly to Eq. (37), is shown in Fig. 8. Both the thermal vorticity and with additional vector-meson contribution (bold lines in Fig. 8) quite well describe the

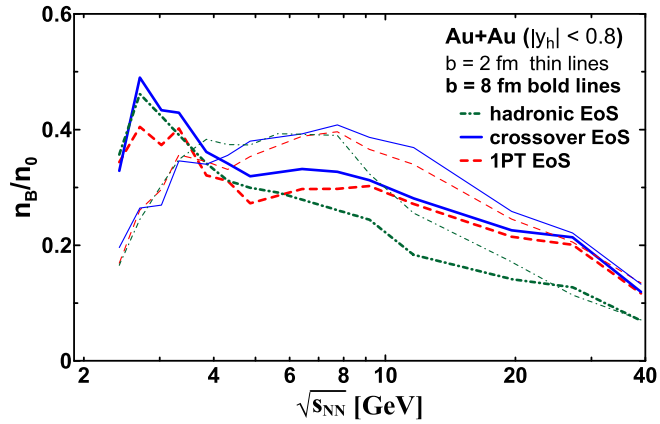

FIG. 7. Mean freeze-out baryon density in units of the normal nuclear density, $n_0 = 0.15$ fm^{-3}, in midrapidity region ($|y_h| < 0.8$) in Au+Au collisions at impact parameters $b = 8$ fm (bold lines) and $b = 2$ fm (thin lines) as function of collision energy $\sqrt{s_{NN}}$. Results for different EoS's are presented.

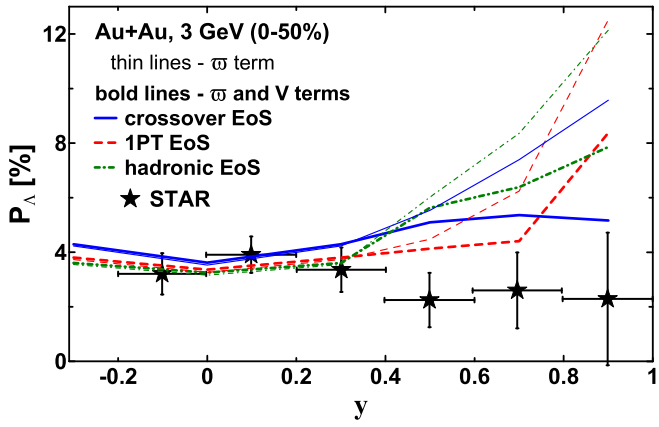

FIG. 8. Rapidity dependence of the global Λ polarization in Au+Au collisions at $\sqrt{s_{NN}} = 3$ GeV (centrality 0–50 %), originated from only the thermal vorticity (thin lines) and with additional vector-meson contribution (bold lines). Results for different EoS's are presented. Data are from Ref. [8] (STAR).

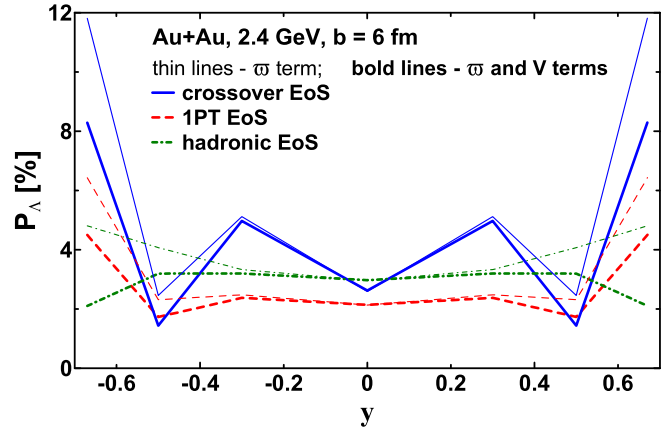

FIG. 10. Rapidity dependence of the global Λ polarization in Au+Au collisions at $\sqrt{s_{NN}} = 2.4$ GeV ($b = 6$ fm), originated from only the thermal vorticity (thin lines) and with additional vector-meson contribution (bold lines). Results for different EoS's are presented.

STAR data [8] at $|y| < 0.3$. However, they overestimate the data at $|y| > 0.3$. The vector-meson contribution somewhat improves the agreement, especially with the crossover EoS, but the overestimation at $|y| > 0.3$ persists.

This observation demonstrates once again that effects of the thermal vorticity and vector-meson interaction become large in rapidity ranges overlapping with the participant-spectator border, see Fig. 6. Moreover, the above contributions produce effects of opposite sign. Therefore, the observed global Λ polarization is a result of a delicate cancellation of the above contributions.

The rapidity dependence of the global Λ polarization at $\sqrt{s_{NN}} = 7.7$ GeV is shown in Fig. 9. It is compared with preliminary STAR data for Au+Au collisions at $\sqrt{s_{NN}} = 7.2$ GeV [9]. The STAR centrality selection is 20–60 %, which corresponds to the impact-parameter range $b = 5.6$–9.7 fm

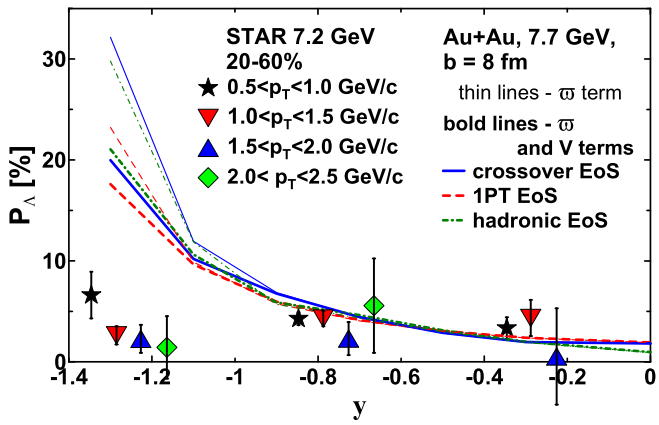

FIG. 9. Rapidity dependence of the global Λ polarization in Au+Au collisions at $\sqrt{s_{NN}} = 7.7$ GeV ($b = 8$ fm), originated from only the thermal vorticity (thin lines) and that with additional vector-meson contribution (bold lines). Results for different EoS's are presented. Preliminary STAR data for Au+Au collisions at $\sqrt{s_{NN}} = 7.2$ GeV and centrality 20–60 % are from Ref. [9].

based on the overlap calculator [49]. Therefore, $b = 8$ fm can be chosen to represent this range. While the STAR data are presented by four subsets corresponding to different selections of transverse momentum, p_T, the 3FD results correspond to averaging over the whole p_T range.

In Fig. 9 we observe the same features as those for $\sqrt{s_{NN}} = 3$ GeV in Fig. 8. The thermal vorticity with or without additional vector-meson contribution well reproduces the STAR data [9] at $|y| < 0.8$ but overestimates the data at $|y| > 0.8$. The vector-meson contribution somewhat reduces the disagreement with data at $|y| > 0.8$.

In Fig. 10 we present our predictions for the ongoing HADES experiment [10]. We avoid modeling Ag+Ag collisions because this system contains of too few particles, especially at low collision energies, to apply the hydrodynamical description. Therefore, we present predictions for the Au+Au collisions at $\sqrt{s_{NN}} = 2.4$ GeV. The results for $b = 6$ fm are shown, which approximately corresponds to centrality 10–40 %. As seen, the basic patterns in Fig. 10 are the same as those in Figs. 8 and 9. Only the difference of the results with different EoS's is larger.

VI. CENTRALITY DEPENDENCE

The global polarization of Λ hyperons in Au+Au collisions is calculated at impact parameters $b = 2$, 4, 6, 8, and 11 fm. The displayed impact parameters are associated with collision centrality by means of the Glauber simulations based on the nuclear overlap calculator [49].

In Fig. 11, centrality dependence of the global Λ polarization in midrapidity region ($|y_h| < 0.8$) in Au+Au collisions at $\sqrt{s_{NN}} = 3$ GeV originated from only the thermal vorticity (thin lines) and with additional vector-meson contribution (bold lines) is displayed. The experimental rapidity window is asymmetric $-0.2 < y < 1$ [8]. However, it well complies with the modeled window in view of flat experimental rapidity dependence of the observed polarization, see Fig. 8. As seen from Fig. 11, both the thermal vorticity and that with

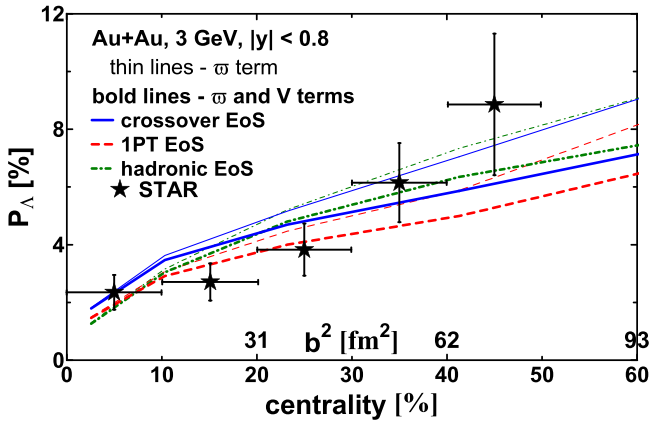

FIG. 11. Centrality dependence of the global Λ polarization in midrapidity region ($|y_h| < 0.8$) in Au+Au collisions at $\sqrt{s_{NN}} = 3$ GeV originated from only the thermal vorticity (thin lines) and with additional vector-meson contribution (bold lines). Results for different EoS's are presented. Data are from Ref. [8].

additional vector-meson contribution reasonably well (though not perfectly) describe the observed centrality dependence.

At the energy of 7.7 GeV, see Fig. 12, the effect of the additional vector-meson contribution becomes negligible because the rapidity window does not cover the regions of the participant-spectator borders, as it has been already discussed in Sec. IV. The thermal vorticity with and without the meson-field contribution reasonably well describes preliminary STAR data for 7.2 GeV energy.

Our predictions for the centrality dependence in Au+Au collisions at $\sqrt{s_{NN}} = 2.4$ GeV (HADES experiment) are presented in Fig. 13. We took the rapidity window $|y_h| < 0.6$, which is similar to that used for the Ag+Ag system in the HADES experiment [10]. Here the situation is similar to that at 3 GeV, see Fig. 11, only the centrality dependence is weaker.

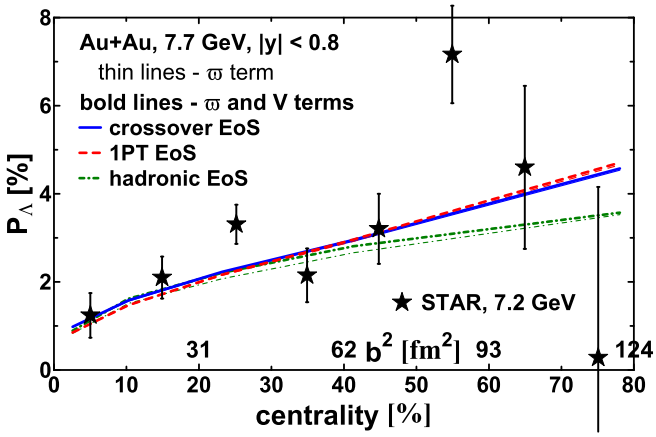

FIG. 12. The same as in Fig. 11 but for $\sqrt{s_{NN}} = 7.7$ GeV. Preliminary STAR data for Au+Au collisions at $\sqrt{s_{NN}} = 7.2$ GeV are from Ref. [9], only statistical errors are displayed.

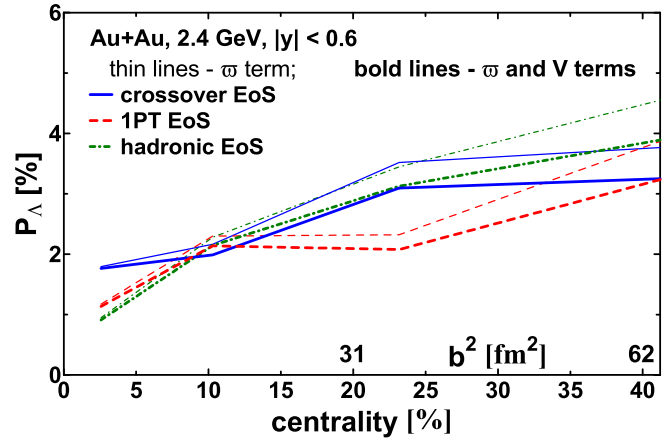

FIG. 13. The same as in Fig. 11 but for the midrapidity region ($|y_h| < 0.6$) at $\sqrt{s_{NN}} = 2.4$ GeV.

VII. EOS

All the above-presented calculations were performed with three EoS's. At moderately relativistic collision energies, $\sqrt{s_{NN}} \lesssim 4.5$ GeV, all these EoS's describe the hadronic matter, except for the crossover EoS containing the small QGP admixture even at low energies. This is seen from Fig. 14, where dynamical trajectories of the matter in the central region of the colliding nuclei in semicentral ($b = 8$ fm) collisions of Au+Au at $\sqrt{s_{NN}} = 2.7, 3.3, 4.9$ GeV are displayed. Only expansion stages of the evolution are displayed. The evolution proceeds from top right to bottom left. Symbols on the trajectories illustrate the expansion rate: they are spaced 1 fm/c apart. The yellow zone in Fig. 14 is a mixed-phase region within the 1PT scenario. The critical temperature

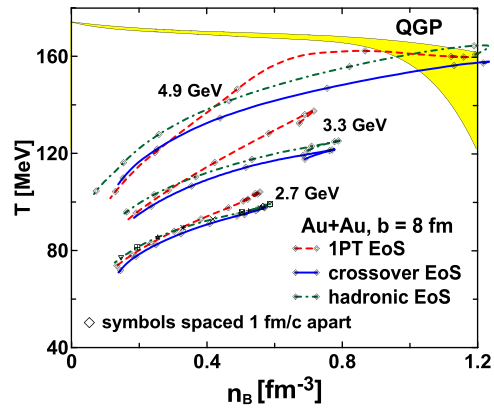

FIG. 14. Dynamical trajectories of the matter in the central box of the colliding nuclei (4 fm × 4 fm × 4 fm/γ_{cm}), where γ_{cm} is the Lorentz factor associated with the initial nuclear motion in the c.m. frame, for semicentral collisions ($b = 8$ fm) of Au+Au at $\sqrt{s_{NN}} =$ 2.7, 3.3, 4.9 GeV. 1PT, crossover and hadronic trajectories are displayed. The trajectories are plotted in terms of baryon density (n_B) and temperature (T). Only expansion stages of the evolution are displayed. Symbols on the trajectories illustrate the expansion rate: they are spaced 1 fm/c apart. The yellow zone is a mixed-phase region within the 1PT scenario.

$T_c = 173$ MeV for the 1PT EoS looks too high nowadays, cf. [67]. This is because the 1PT and crossover EoS's in Ref. [20] were fitted to old, still imperfect lattice data [68–70]. However, this shortcoming is not severe for the reproduction of bulk observables in heavy-ion collisions.

In spite of that all the considered EoS's describe the hadronic matter at moderately relativistic collision energies, they are not identical. Indeed, the corresponding dynamical trajectories in the hadronic phase are different, see Fig. 14, though close to each other. Therefore, differences in predictions of these EoS's can be considered as an uncertainty resulting from EoS ambiguity in the hadronic phase. All the considered EoS's give almost identical predictions for bulk [21,71–73] and even flow [74–76] observables at moderately relativistic collision energies. The polarization turns out to be more sensitive to details of the EoS.

VIII. SUMMARY

Based on the 3FD model, the global Λ polarization in Au+Au collisions at moderately relativistic energies, $2.4 \leqslant \sqrt{s_{NN}} \leqslant 7.7$ GeV, was calculated, including its rapidity and centrality dependence. Contributions of the thermal vorticity and meson-field interaction [51] to the global polarization were considered. Feed down from higher-lying resonances was also studied, which as found reduces the polarization by $\approx$25% at lower energies and by $\approx$15% at 7.7 GeV. The results were compared with data from recent and ongoing experiments [8–10]. It is predicted that the global polarization increases with the collision energy decrease. A maximum is reached at $\sqrt{s_{NN}} \approx 3$ GeV, if the measurements are performed with the same acceptance.

The value of the polarization is very sensitive to interplay of the aforementioned different contributions. In particular, the thermal vorticity predicts quite strong increase of the polarization from the midrapidity to forward/backward rapidities, while the meson-field contribution considerably flattens the rapidity dependence. The meson-field contribution is large at the participant-spectator border and hence considerably reduces the polarization at forward/backward rapidities, while it is practically negligible at the midrapidity. As a rule, it improves agreement of calculated polarization with available data. Note that one of many possible parametrizations of the meson-field interaction was used in the present calculations. It indicates the order of magnitude and character of the produced effect. The details may be different for other, more refined parametrizations, e.g., such as those developed in Refs. [64,77,78] for astrophysical applications.

The simulations were performed with three different EoS's. In spite of that, all the considered EoS's describe the hadronic matter at $\sqrt{s_{NN}} \lesssim 4.5$ GeV, they are not identical. The polarization turns out to be more sensitive to details of the EoS than bulk and even flow observables. The EoS crossover is somewhat preferable, although the data reproduction is far from being perfect. This could be a result of imperfectness of the crossover EoS, in view of high sensitivity of the global polarization to the EoS. Alternatively, this may indicate that the effect of the thermal-shear contribution [79–81] should be additionally explored. Authors of Ref. [29] found that at the energy of 19.6 GeV the effect of the thermal shear is negligibly small at the freeze-out stage. Whether this is so at moderately relativistic energies remains to be seen.

All presently available approaches to the particle polarization, i.e., the thermodynamic approach used here [16–18] and that based on the chiral-vortical effect [82–87], require the thermal equilibrium at the freeze-out stage. At the same time the collision dynamics becomes less and less equilibrium with the collision energy decrease. This becomes a problem at low energies. We argue that the equilibrium is achieved at the freeze-out stage, only this equilibration takes longer.

ACKNOWLEDGMENTS

Helpful discussions with E. E. Kolomeitsev and D. N. Voskresensky are gratefully acknowledged. This work was carried out using computing resources of the federal collective usage center "Complex for simulation and data processing for mega-science facilities" at NRC "Kurchatov Institute" [88]. Y.B.I. was partially supported by the Russian Foundation for Basic Research, Grants No. 18-02-40084 and No. 18-02-40085. This work was also supported by MEPhI within the Federal Program "Priority-2030".

[1] L. Adamczyk *et al.* (STAR Collaboration), Nature (London) **548**, 62 (2017).
[2] J. Adam *et al.* (STAR Collaboration), Phys. Rev. C **98**, 014910 (2018).
[3] J. Adam *et al.* (STAR Collaboration), Phys. Rev. Lett. **126**, 162301 (2021).
[4] J. Adam *et al.* (STAR Collaboration), Phys. Rev. Lett. **123**, 132301 (2019).
[5] X. G. Deng, X. G. Huang, Y. G. Ma, and S. Zhang, Phys. Rev. C **101**, 064908 (2020).
[6] Y. B. Ivanov, Phys. Rev. C **103**, L031903 (2021).
[7] Y. Guo, J. Liao, E. Wang, H. Xing, and H. Zhang, Phys. Rev. C **104**, L041902 (2021).
[8] M. S. Abdallah *et al.* (STAR Collaboration), Phys. Rev. C **104**, L061901 (2021).
[9] K. Okubo (STAR Collaboration), EPJ Web Conf. **259**, 06003 (2022).
[10] F. Kornas (HADES Collaboration), Talk given at StrangeQuark Matter 2021, Online Conference, May 17–22, 2021. https://indico.cern.ch/event/985652/contributions/4305142/attachments/2246397/; F. J. Kornas, doi:10.26083/tuprints-00019763.
[11] K. Meehan (STAR Collaboration), Nucl. Phys. A **967**, 808 (2017).
[12] G. Agakishiev *et al.* (HADES Collaboration), Eur. Phys. J. A **41**, 243 (2009).
[13] T. Ablyazimov *et al.* (CBM Collaboration), Eur. Phys. J. A **53**, 60 (2017).
[14] V. D. Kekelidze, V. A. Matveev, I. N. Meshkov, A. S. Sorin, and G. V. Trubnikov, Phys. Part. Nucl. **48**, 727 (2017).

[15] Y. B. Ivanov, V. N. Russkikh, and V. D. Toneev, Phys. Rev. C **73**, 044904 (2006).
[16] F. Becattini, V. Chandra, L. Del Zanna, and E. Grossi, Ann. Phys. (NY) **338**, 32 (2013).
[17] F. Becattini, I. Karpenko, M. A. Lisa, I. Upsal, and S. A. Voloshin, Phys. Rev. C **95**, 054902 (2017).
[18] R.-H. Fang, L.-G. Pang, Q. Wang, and X.-N. Wang, Phys. Rev. C **94**, 024904 (2016).
[19] I. N. Mishustin, V. N. Russkikh, and L. M. Satarov, Sov. J. Nucl. Phys. **54**, 260 (1991).
[20] A. S. Khvorostukhin, V. V. Skokov, K. Redlich, and V. D. Toneev, Eur. Phys. J. C **48**, 531 (2006).
[21] Y. B. Ivanov, Phys. Rev. C **87**, 064904 (2013).
[22] I. Karpenko and F. Becattini, Eur. Phys. J. C **77**, 213 (2017).
[23] Y. L. Xie, M. Bleicher, H. Stöcker, D. J. Wang, and L. P. Csernai, Phys. Rev. C **94**, 054907 (2016).
[24] Y. Xie, D. Wang, and L. P. Csernai, Phys. Rev. C **95**, 031901(R) (2017).
[25] Y. B. Ivanov, V. D. Toneev, and A. A. Soldatov, Phys. Rev. C **100**, 014908 (2019).
[26] Y. B. Ivanov, V. D. Toneev, and A. A. Soldatov, Phys. At. Nucl. **83**, 179 (2020).
[27] Y. B. Ivanov and A. A. Soldatov, Phys. Rev. C **102**, 024916 (2020).
[28] B. Fu, K. Xu, X. G. Huang, and H. Song, Phys. Rev. C **103**, 024903 (2021).
[29] Y. Sun, Z. Zhang, C. M. Ko, and W. Zhao, arXiv:2112.14410.
[30] H. Li, L. G. Pang, Q. Wang, and X. L. Xia, Phys. Rev. C **96**, 054908 (2017).
[31] Y. Sun and C. M. Ko, Phys. Rev. C **96**, 024906 (2017).
[32] D. X. Wei, W. T. Deng, and X. G. Huang, Phys. Rev. C **99**, 014905 (2019).
[33] S. Shi, K. Li, and J. Liao, Phys. Lett. B **788**, 409 (2019).
[34] E. E. Kolomeitsev, V. D. Toneev, and V. Voronyuk, Phys. Rev. C **97**, 064902 (2018).
[35] O. Vitiuk, L. V. Bravina, and E. E. Zabrodin, Phys. Lett. B **803**, 135298 (2020).
[36] A. Lei, D. Wang, D. M. Zhou, B. H. Sa, and L. P. Csernai, Phys. Rev. C **104**, 054903 (2021).
[37] F. Becattini and M. A. Lisa, Annu. Rev. Nucl. Part. Sci. **70**, 395 (2020).
[38] I. Karpenko, in *Strongly Interacting Matter under Rotation*, edited by F. Becattini, J. Liao, and M. Lisa, Lecture Notes in Physics Vol 987 (Springer, Cham).
[39] Y. B. Ivanov and A. A. Soldatov, Phys. Rev. C **101**, 024915 (2020).
[40] Y. B. Ivanov and A. A. Soldatov, Eur. Phys. J. A **52**, 367 (2016).
[41] L. V. Bravina, I. Arsene, M. S. Nilsson, K. Tywoniuk, E. E. Zabrodin, J. Bleibel, A. Faessler, C. Fuchs, M. Bleicher, G. Burau, and H. Stöcker, Phys. Rev. C **78**, 014907 (2008).
[42] H. Petersen, J. Steinheimer, G. Burau, M. Bleicher, and H. Stocker, Phys. Rev. C **78**, 044901 (2008).
[43] S. De, S. De, and S. Chattopadhyay, Phys. Rev. C **94**, 054901 (2016).
[44] M. Teslyk, L. Bravina, O. Panova, O. Vitiuk, and E. Zabrodin, Phys. Rev. C **101**, 014904 (2020).
[45] D. Oliinychenko and H. Petersen, Phys. Rev. C **93**, 034905 (2016).
[46] A. Andronic, P. Braun-Munzinger, and J. Stachel, Nucl. Phys. A **772**, 167 (2006).
[47] V. N. Russkikh and Yu. B. Ivanov, Phys. Rev. C **76**, 054907 (2007).
[48] Y. B. Ivanov and V. N. Russkikh, Phys. At. Nucl. **72**, 1238 (2009).
[49] http://web-docs.gsi.de/~misko/overlap/interface.html
[50] B. I. Abelev *et al.* (STAR Collaboration), Phys. Rev. C **79**, 034909 (2009).
[51] L. P. Csernai, J. I. Kapusta, and T. Welle, Phys. Rev. C **99**, 021901(R) (2019).
[52] Y. Xie, G. Chen, and L. P. Csernai, Eur. Phys. J. C **81**, 12 (2021).
[53] J. D. Walecka, Ann. Phys. (NY) **83**, 491 (1974).
[54] B. D. Serot and J. D. Walecka, Adv. Nucl. Phys. **16**, 1 (1986); B. D. Serot, Rep. Prog. Phys. **55**, 1855 (1992); B. D. Serot and J. D. Walecka, Int. J. Mod. Phys. E **06**, 515 (1997).
[55] J. I. Kapusta and C. Gale, *Finite Temperature Field Theory* (Cambridge University Press, Cambridge, 2006).
[56] L. L. Foldy and S. A. Wouthuysen, Phys. Rev. **78**, 29 (1950).
[57] J. D. Bjorken and S. D. Drell, *Relativistic Quantum Mechanics* (McGraw-Hill, New York, 1964).
[58] W. Greiner, *Relativistic Quantum Mechanics* (Springer-Verlag, Berlin, 1987).
[59] Y. B. Ivanov and A. A. Soldatov, Phys. Rev. C **97**, 044915 (2018).
[60] X. L. Xia, H. Li, Z. B. Tang, and Q. Wang, Phys. Rev. C **98**, 024905 (2018).
[61] M. A. Lisa, J. G. Prado Barbon, D. D. Chinellato, W. M. Serenone, C. Shen, J. Takahashi, and G. Torrieri, Phys. Rev. C **104**, L011901 (2021).
[62] F. Becattini and F. Piccinini, Ann. Phys. (NY) **323**, 2452 (2008).
[63] S. Weissenborn, D. Chatterjee, and J. Schaffner-Bielich, Phys. Rev. C **85**, 065802 (2012); **90**, 019904(E) (2014).
[64] K. A. Maslov, E. E. Kolomeitsev, and D. N. Voskresensky, Nucl. Phys. A **950**, 64 (2016).
[65] J. Cohen and H. J. Weber, Phys. Rev. C **44**, 1181 (1991)
[66] J. Randrup and J. Cleymans, Phys. Rev. C **74**, 047901 (2006).
[67] S. Borsanyi, G. Endrodi, Z. Fodor, S. D. Katz, S. Krieg, C. Ratti, and K. K. Szabo, J. High Energy Phys. 08 (2012) 053.
[68] Z. Fodor, Nucl. Phys. A **715**, 319c (2003).
[69] F. Csikor, G. I. Egri, Z. Fodor, S. D. Katz, K. K. Szabo, and A. I. Toth, J. High Energy Phys. 05 (2004) 046.
[70] F. Karsch, E. Laermann, and A. Peikert, Nucl. Phys. B **605**, 579 (2001).
[71] Y. B. Ivanov, Phys. Rev. C **87**, 064905 (2013).
[72] Y. B. Ivanov, Phys. Rev. C **89**, 024903 (2014).
[73] Y. B. Ivanov and A. A. Soldatov, Phys. Rev. C **97**, 024908 (2018).
[74] Y. B. Ivanov and A. A. Soldatov, Phys. Rev. C **91**, 024914 (2015).
[75] V. P. Konchakovski, W. Cassing, Y. B. Ivanov, and V. D. Toneev, Phys. Rev. C **90**, 014903 (2014).
[76] Y. B. Ivanov and A. A. Soldatov, Phys. Rev. C **91**, 024915 (2015).
[77] K. A. Maslov, E. E. Kolomeitsev, and D. N. Voskresensky, Phys. Lett. B **748**, 369 (2015).
[78] N. Hornick, L. Tolos, A. Zacchi, J. E. Christian, and J. Schaffner-Bielich, Phys. Rev. C **98**, 065804 (2018); **103**, 039902 (2021).
[79] F. Becattini, M. Buzzegoli, and A. Palermo, Phys. Lett. B **820**, 136519 (2021).
[80] S. Y. F. Liu and Y. Yin, J. High Energy Phys. 07 (2021) 188.

[81] F. Becattini, M. Buzzegoli, A. Palermo, G. Inghirami, and I. Karpenko, Phys. Rev. Lett. **127**, 272302 (2021).
[82] A. Vilenkin, Phys. Rev. D **21**, 2260 (1980).
[83] D. T. Son and A. R. Zhitnitsky, Phys. Rev. D **70**, 074018 (2004).
[84] J. H. Gao, Z. T. Liang, S. Pu, Q. Wang, and X. N. Wang, Phys. Rev. Lett. **109**, 232301 (2012).
[85] A. Sorin and O. Teryaev, Phys. Rev. C **95**, 011902(R) (2017).
[86] M. Baznat, K. Gudima, A. Sorin, and O. Teryaev, Phys. Rev. C **97**, 041902(R) (2018).
[87] Y. B. Ivanov, Phys. Rev. C **102**, 044904 (2020).
[88] http://ckp.nrcki.ru/.